A brick model for asperity sintering and creep of APS TBCs

Alan Cocks [a,*], Norman Fleck [b] and Stefan Lampenscherf [c]

[a] Department of Engineering Science, University of Oxford, Parks Road, Oxford OX1 3PJ, UK
[b] Cambridge University Engineering Department, Trumpington Street, Cambridge CB2 1PZ, UK
[c] Siemens AG, Corporate Technology, Otto-Hahn-Ring 6, D-81730, München, Germany

15 August 2012

Keywords: Thermal Barrier Coating, Air Plasma Sprayed, Sintering, Creep, Micromechanical, Transversely Isotropic.

Abstract

A micromechanical model is developed for the microstructural evolution of an air plasma sprayed (APS), thermal barrier coating: discrete, brick-like splats progressively sinter together at contacting asperities and also undergo Coble creep within each splat. The main microstructural features are captured: the shape, orientation and distribution of asperities between splats, columnar grains within each splat and the disc-shaped splats. Elasticity is accounted for at the asperity contacts and within each splat, and the high contact compliance explains the fact that APS coatings have a much lower modulus (and thermal conductivity) than that of the parent, fully dense solid. The macroscopic elastic, sintering and creep responses are transversely isotropic, and remain so with microstructural evolution. Despite the large number of geometric and kinetic parameters, the main features of the behaviour are captured by a small number of characteristic material timescales: these reveal the competition between the deformation mechanisms and identify the rate controlling processes for both free and constrained sintering. The evolution of macroscopic strain, moduli and asperity size is compared for free and constrained sintering, and the level of in-plane stress within a constrained coating is predicted.

*Corresponding author: Tel. +44 1865 283490
E-mail address: alan.cocks@eng.ox.ac.uk

1. Introduction

Air plasma sprayed (APS) thermal barrier coatings (TBCs) are used extensively as protective thermal barriers of creep resistant stationary parts in land-based gas turbines. The APS coating comprises an assembly of zirconia splats, with intervening cracks and porosity, as shown in Fig. 1. Typically, the TBC layer is of thickness 300-500μm, but a much wider range is achievable, see for example Cernuschi et al. (2008). The coating sits on an aluminium-rich bond coat (BC) of thickness 150-300μm. Each splat has a height $2h$ of about 1 μm, and a radius R of 10-50μm. The splats have a characteristic internal microstructure: they comprise columnar grains of diameter d equal to 0.1 – 0.2μm. Porosity also exists, of volume fraction about 15% and diameter 1–20μm. The effect of voids upon the modulus and thermal conductivity is minor, as discussed by Sevostianov *et al.* (2004).

Recall that the main function of the APS coating is to provide a thermal barrier between the hot engine gas and the underlying creep-resistant superalloy. The presence of interfaces between the splats of the coating is advantageous as they reduce the thermal conductivity of the zirconia layer and they thereby enhance the performance of the thermal barrier coating. Additionally, these partially-sintered interfaces reduce the effective Young's modulus of the coating and thereby reduce the level of in-plane thermal stress within the coating. The details are as follows. The in-plane thermal expansion coefficient of the coating, α_{TBC} = 10 x 10^{-6} K^{-1}, is significantly less than that of the underlying nickel-based superalloy, α_{Ni} = 15 x 10^{-6} K^{-1}. A sudden temperature excursion of coating and substrate will induce elastic strains within the coating, and thereby generate thermal stresses which scale with the in-plane modulus of the TBC layer. The initial in-plane modulus of the TBC layer E_{TBC} is on the order of 40GPa, and may double over the life of the coating due to sintering of the inter-splat asperities; this leads to the possibility of coating delamination during cool-down. The asperity sintering is driven by in-plane stress within the coating and by the surface energy $\gamma_{\mathrm{SUR}} \approx 1 \mathrm{Jm}^{-2}$ of the zirconia.

Some of the above features of sintering of APS coatings have been modelled by Cipitria et al. (2009a,b). They construct a periodic 3D unit cell, with a single "bridge contact" across adjacent splats. Consequently, the diffusion distances are on the order of the splat size. Also, the macroscopic modulus is held fixed as sintering of the

bridge contacts progresses. In contrast, Erikkson et al (2012) have recently observed that splats are in contact at discrete asperities on their surfaces and emphasise that these asperities progressively enlarge in their burner-rig tests. Nonetheless, the model developed by Cipitria et al. (2009a,b) has been successfully used by Takagi et al (2011) to interpret their measurements of sintering shrinkage in APS coatings.

Recently, Fleck and Cocks (2009) introduced a sintering model for APS TBCs. The gaps between individual splats are represented by a random 3D distribution of planar, circular microcracks, with asperities bridging the faces of each crack. Macroscopic inelastic straining arises from a combination of Coble creep of the APS splats, and asperity-sintering of the inter-splat cracks. The model also provides relationships for the evolution of elastic properties as the coating sinters. This isotropic model is in the spirit of a *stage II sintering* model for particulate systems (Ashby (1974)) and is physically realistic when the porosity and microcracks are isolated.

An alternative perspective is adopted in the present study that is consistent with the observations of Erikkson et al (2012). As-deposited TBC coatings contain an assembly of discrete splats which are bridged by asperities. At elevated temperature the asperity contacts grow and the initial sintering response is similar to that of *stage I sintering* of a powder compact, see for example Ashby (1974). This is reinforced by the observation that the initial in-plane modulus is about one fifth that of fully dense zirconia (and only increases to two-fifths over the life of the coating). Models based on a distribution of isolated cracks or voids give much higher moduli (unless these defects are at the percolation limit), see Fleck and Cocks (2009).

2. A brick model for creep and sintering

The present development is concerned with a *stage I* sintering model for APS TBCs: we assume that the coating behaves as an assembly of layered hexagonal bricks. The bricks are sintered to each other by discrete asperities at the contacting faces. Additionally, the bricks undergo Coble creep and elastic straining due to bulk elastic deformation of the bricks and the finite compliance of the asperities. As asperity sintering progresses, the stiffness of each asperity increases and this leads to an increase in macroscopic moduli. The degree of anisotropy is closely linked to the shape and arrangement of bricks. We shall limit attention to (i) free sintering and (ii) constrained sintering of the TBC, where the response of the coating is transversely

isotropic. For such problems it suffices to model the bricks as an arrangement of regular hexagons in layers of height $2h$. The elastic compliance of the coating is taken to be the sum of the compliance of each brick and that of the asperity contacts.

2.1 The splat and asperity geometry

We perform two levels of idealisation of the TBC geometry, as follows. First, we envisage a space-filling arrangement of regular hexagonal splats in the (1, 2) plane, as shown in Fig. 2. Each splat is of side-length *L*, and of height 2*h* in the 3-direction. It is envisaged that the splats have local order so that they pack face-to-face, but they possess no long-range order of in-plane orientation. This motivates the second level of approximation: we replace a representative hexagonal splat (of cross-sectional area $A = 3\sqrt{3}L^2/2$) by an equivalent circular splat of radius *R* and of the same cross-sectional area *A*, implying that $R = 0.91L$. Likewise, the hexagonal arrangement of face-contacts between the representative hexagon to its neighbours is replaced by inter-splat contacts around the periphery of the equivalent circular splat. (The notion of an equivalent circular grain was also adopted by Coble (1963) in creep problems, and by Ashby (1974) in stage I sintering problems.)

Now consider a representative unit cell of 3 splats, labelled, 0, 1 and 2. We assume that a representative interface between splats has a random orientation ***N***, as shown in Figs. 3 and 4. The normal ***N*** resides within the $(\boldsymbol{e}_1, \boldsymbol{e}_2)$ plane at a random angle θ to the $\boldsymbol{e}_1$ direction, such that

$$\boldsymbol{N} = \boldsymbol{e}_1 \cos\theta + \boldsymbol{e}_2 \sin\theta \qquad (2.1)$$

Assume that the side-faces of the splats are sintered to neighbouring splats by isolated circular, cylindrical asperities of top-hat shape, consistent with the recent experimental observations by Erikkson et al (2012) as described in the Introduction. Each asperity is of height w^{S}, radius b^{S} and average spacing ℓ^{S}, such that the number of contacts per unit area is $m^{\mathrm{S}} = \frac{4}{\pi}\left(\ell^{\mathrm{S}}\right)^{-2}$. Since we are primarily interested in applications such as constrained sintering upon a substrate, we can assume a transversely isotropic response: consequently, we assume that (b^{S}, w^{S}, ℓ^{S}) do not depend upon direction within the plane of the splat. Likewise, assume that the top and bottom of the splats are sintered to neighbouring splats at asperities. Each asperity has the same height

w^{T}, radius b^{T} and average spacing ℓ^{T}, such that the number of contacts per unit area is $m^{\mathrm{T}} = \frac{4}{\pi}\left(\ell^{\mathrm{T}}\right)^{-2}$. We proceed to derive a multi-axial constitutive model for the APS coating, with w^{S} and w^{T} serving the role of internal state variables that evolve with time. The quantities b^{S} and b^{T} are kinematically linked to w^{S} and w^{T}, respectively, by conservation of volume of the asperities.

In reality, the splats are not perfectly stacked and the TBC has a greater shear stiffness and strength than that assumed by hexagonal bricks with flat and parallel tops and bottoms. This is addressed by assuming that the contacts formed by the asperities at the top and bottom of the splats have a unit normal $\boldsymbol{n}$ that is inclined at some random azimuthal angle ϕ to the direction $\boldsymbol{e}_3$ up to a maximum misalignment angle of ω. Additionally, the component of $\boldsymbol{n}$ within the $(\boldsymbol{e}_1, \boldsymbol{e}_2)$ plane is randomly orientated such that the polar angle ψ lies in the range 0 to 2π with respect to the $\boldsymbol{e}_1$ direction. Then, we can write

$$\boldsymbol{n} = \boldsymbol{e}_1 \sin\phi\cos\psi + \boldsymbol{e}_2 \sin\phi\sin\psi + \boldsymbol{e}_3 \cos\phi \qquad (2.2)$$

For simplicity, we shall assume that (b^{T}, w^{T}, ℓ^{T}) are independent of the orientation (ϕ, ψ), but can be different from the values at the side of the splat. We emphasise that the asperity size, but not the asperity spacing, can evolve due to local sintering.

It is assumed that the overall elastic compliance arises from elastic straining of each splat (taken to be the same as that of the fully dense bulk) and from elastic deformation of the asperities. Additionally, the inelastic response is taken to be the sum of the Coble creep deformation of each splat (as given by that of the fully dense bulk) and the additional contribution from sintering of the asperities. In the following sub-sections we consider each of these contributions in turn, and it is clear from the context whether the macroscopic strain arises from sintering, Coble creep or from elastic deformation. In section 5, the three contributions to macroscopic strain are combined, and notation is introduced to identify the three distinct contributions to the macroscopic response.

3. Macroscopic response due to sintering of the asperities

3.1 Macro-micro relationships

We assume affine deformation in order to connect macroscopic straining to the local sintering response, and use the Principle of Virtual Work to calculate the macroscopic stress Σ_{ij} associated with any assumed macroscopic strain rate $\dot{E}_{ij}$. The details are as follows.

Consider the representative splat arrangement of Fig. 3a. The local displacement rate between particles 0 and 1, across a side contact with outward normal ***N***, is related to the macroscopic strain rate by

$$\dot{u}_\alpha^{\mathrm{S}} = 2\dot{E}_{\alpha\beta}N_\beta R \tag{3.1}$$

where (α, β) are in the range (1,2). Similarly, the relative displacement rate between particles 0 and 2 across the top face is

$$\dot{u}_i^{\mathrm{T}} = \dot{E}_{i\beta}N_\beta R + 2\dot{E}_{i3}h \tag{3.2}$$

Note our notation: a superscript S denotes side of splat, while a superscript T denotes top of splat.

The inter-splat velocity $\dot{u}_N^{\mathrm{S}}$ gives rise to a contact force f_N^{S} at each asperity on the side-face of the representative splat 0. Similarly, the inter-splat velocity $\dot{u}_i^{\mathrm{T}}$ gives rise to a contact force f_i^{T} at each asperity on the top and bottom faces of splat 0. The Principle of Virtual Work then gives

$$\Sigma_{ij}\delta\dot{E}_{ij}V = \frac{1}{2}\left[\int_{S^{\mathrm{T}}} m^{\mathrm{T}} f_i^{\mathrm{T}}\delta\dot{u}_i^{\mathrm{T}} dS + \int_{S^{\mathrm{S}}} m^{\mathrm{S}} f_N^{\mathrm{S}}\delta\dot{u}_N^{\mathrm{S}} dS\right] \tag{3.3}$$

where $V = 2\pi R^2 h$ is the splat volume, $S^{\mathrm{T}} = 2\pi R^2$ is the top and bottom area and $S^{\mathrm{S}} = 4\pi Rh$ is the side area. The factor of ½ arises because the asperities are shared between two splats. The next step is to derive expressions for (f_N^{S}, f_i^{T}) in terms of ($\dot{u}_N^{\mathrm{S}}$, $\dot{u}_i^{\mathrm{T}}$).

3.2 The sintering response of a single asperity

Consider the generic problem of sintering of a single circular cylindrical asperity, of radius *b* and height *w*. It is envisaged that the asperity straddles two flat, parallel surfaces, and exists either at the side face of a splat or along the top and bottom faces, as shown in Fig. 3. It is assumed that matter diffuses along the top of each asperity, and deposits along the free surfaces of height *w*. Matter diffuses from the sides of asperities, of local surface energy γ_{SUR} to contacts with interfacial energy γ_{G}. Take as the reference free energy a state consisting of two separated parallel splat surfaces. Introduction of a single asperity, under a prescribed tensile force *f* across the asperity, leads to an increase in free surface energy of

$$G_a = \pi b^2 \left(\gamma_{\mathrm{G}} - 2\gamma_{\mathrm{SUR}}\right) + 2\pi b w \gamma_{\mathrm{SUR}} - fw \tag{3.4}$$

The rate potential Ψ_a for each asperity is given by (A3) of Cocks and Fleck (2010), and reads in the present notation as

$$\Psi_a = \left[\frac{\pi}{16}\frac{b^4}{D_{\mathrm{G}}} + \frac{\pi}{12}\frac{wb^3}{D_{\mathrm{SUR}}}\right]\dot{w}^2 \tag{3.5}$$

where D_{G} and D_{SUR} are the diffusion constants for grain boundary and surface diffusion, respectively. The rate quantity $\dot{w}$ is obtained by minimising the functional $\Omega_a\left(\dot{w}\right) \equiv \dot{G}_a + \Psi_a$, where $\dot{G}_a$ is obtained by differentiating (3.4) with respect to time, and is linear in $\dot{w}$. The minimisation results in the single algebraic equation

$$f = \lambda \dot{w} + f_{\mathrm{SIN}} \tag{3.6}$$

in terms of an asperity viscosity

$$\lambda = \frac{\pi}{8}\frac{b^4}{D_{\mathrm{G}}} + \frac{\pi}{6}\frac{wb^3}{D_{\mathrm{SUR}}} \tag{3.7}$$

and a sintering force

$$f_{\mathrm{SIN}} = \pi b \gamma_{\mathrm{SUR}} + \pi\left(2\gamma_{\mathrm{SUR}} - \gamma_{\mathrm{G}}\right)\frac{b^2}{w} \tag{3.8}$$

3.3 Deformation at the scale of the splats

Relative motion of the splats is accommodated by sintering and free sliding of the asperities on the sides, top and bottom surfaces of each splat. The relative motion induces work-conjugate contact forces on each asperity. We determine first the

normal force on a typical asperity on the side-face of a splat, and second the normal force on an asperity on the top face. The tangential components are zero due to the assumption of free sliding.

Consider a representative splat, such as element 0 of Fig 3, which is in contact with splat 2 along a common side face with outward normal ***N***. The normal component of inter-splat velocity $\dot{u}_N^{\mathrm{S}} = \dot{u}_\alpha^{\mathrm{S}} N_\alpha = \dot{w}^{\mathrm{S}}$ induces a local asperity contact force in accordance with (3.6), such that

$$f_\alpha^{\mathrm{S}} = \lambda^{\mathrm{S}} N_\alpha N_\beta \dot{u}_\beta^{\mathrm{S}} + f_{\mathrm{SIN}}^{\mathrm{S}} N_\alpha \tag{3.9a}$$

for $(\alpha, \beta) = (1, 2)$ and

$$f_3^{\mathrm{S}} = 0 \tag{3.9a}$$

Here, λ^{S} and $f_{\mathrm{SIN}}^{\mathrm{S}}$ are given by eqns (3.7) and (3.8), with *b* and *w* interpreted as b^{S} and w^{S}, respectively.

The contacting surfaces of asperities at the top and bottom of a splat are not perfectly horizontal. Rather, the outward normal ***n*** at each contact on the top surface of splat 0 of Fig 3 is given by eqn (2.2), where the azimuthal angle ϕ has a *random* value in the range 0 to ω; likewise, the polar angle ψ has a random value in the range of 0 to 2π. This problem is considered in Appendix A, where we assume that there is no preferred orientation of asperities for ψ within the range 0 to ω, so that all possible orientations occur with equal probability. The average contact force for an asperity is determined via a virtual work calculation as detailed in Appendix A. The average force per asperity is given by

$$f_\alpha^{\mathrm{T}} = \lambda^{\mathrm{T}} \dot{u}_\alpha^{\mathrm{T}} g_1(\omega) \tag{3.10}$$

for $\alpha = 1, 2$ and

$$f_3^{\mathrm{T}} = \lambda^{\mathrm{T}} \dot{u}_3^{\mathrm{T}} g_2(\omega) + f_{\mathrm{SIN}}^{\mathrm{T}} g_3(\omega) \tag{3.11}$$

where the superscript T again indicates a quantity associated with the top (or bottom) surface of a splat and λ^{T} and $f_{\mathrm{SIN}}^{\mathrm{T}}$ are given by eqns (3.7) and (3.8), respectively.

Likewise, b and w are interpreted as b^{T} and w^{T}. The geometric parameters (g_1, g_2, g_3) are given by integration of (A2) and are re-stated here as

$$\left.\begin{aligned} g_1(\omega) &= \tfrac{1}{6}\left(2-\cos\omega-\cos^2\omega\right) \\ g_2(\omega) &= \tfrac{1}{3}\left(1+\cos\omega+\cos^2\omega\right) \\ g_3(\omega) &= \tfrac{1}{2}\left(1+\cos\omega\right) \end{aligned}\right\} \qquad (3.12)$$

Note that for $\omega = 0$, we have $f_\alpha^{\mathrm{T}} = g_1(\omega) = 0$, and (3.11) reduces to (3.6).

3.4 Application of Virtual Work Principle to deduce macroscopic stress

The macroscopic stress Σ_{ij} is determined by substitution of (3.1), (3.2) and (3.9-3.11) into the Principle of Virtual Work (3.3). After some rearrangement, the macroscopic stress reads

$$\Sigma_{ij} = \Lambda_{ijkl}\dot{E}_{kl} + \Sigma_{ij}^{\mathrm{SIN}} \qquad (3.13)$$

where the viscosity tensor Λ_{ijkl} is transversely isotropic, with components given explicitly in Appendix B. The macroscopic sintering stress has three non-zero components

$$\Sigma_{11}^{\mathrm{SIN}} = \Sigma_{22}^{\mathrm{SIN}} = f_{\mathrm{SIN}}^{\mathrm{S}} m^{\mathrm{S}} \qquad \text{and} \qquad \Sigma_{33}^{\mathrm{SIN}} = g_3(\omega)\, f_{\mathrm{SIN}}^{\mathrm{T}} m^{\mathrm{T}} \qquad (3.14)$$

Inversion of (3.13) gives

$$\dot{E}_{ij} = \Lambda_{ijkl}^{-1}\left(\Sigma_{kl} - \Sigma_{kl}^{\mathrm{SIN}}\right) \qquad (3.15)$$

At some stage in the sintering process the asperities on the sides and tops of the splats will merge to form a continuous interface. In general, the top and side asperities will fully sinter at different times. When a given family of asperities fully sinter, there is no further evolution of interface area and energy and there is no longer a contribution to the sintering stress associated with this family of asperities, ie either $\Sigma_{11}^{\mathrm{SIN}} = \Sigma_{22}^{\mathrm{SIN}} = 0$ or $\Sigma_{33}^{\mathrm{SIN}} = 0$. Also the component of the viscosity due to asperity sintering normal to the splat surface that has fully sintered goes to infinity.

Sintering of the side asperities is accommodated by sliding at the top and bottom of the splats. When ω>0, sliding is, in turn, accommodated by sintering of the top and

bottom asperities. This results in the top asperities contributing to the in-plane viscosities Λ_{1111}, Λ_{2222} (as shown in the first of eqns B1 of Appendix B). Consider the situation where the top and bottom asperities fully sinter before the side asperities. This creates a non-planar interface between the splats with the azimuthal angle ϕ of the normal to the interface varying randomly within the range 0 to ω. We assume that the interface consists of randomly orientated circular patches of diameter ℓ^{T} and that the local component of the velocity resulting from sliding at the splat interface is uniform across the patch, resulting in a local radial flux pattern. Volume of material must also be conserved at the sliding interface. Applying the Principle of Virtual Work and imposing this constraint gives the same expressions for the in-plane viscosities Λ_{1111}, Λ_{2222} that are given in Appendix B.

4. The contribution to macroscopic compliance due to elastic deformation of the asperities

Recall that the measured in-plane modulus of a typical APS coating is much less than that of fully dense zirconia (by a factor of about five). Consequently, the dominant contribution to macroscopic *compliance* is the elastic deformation of asperities between splats. Since we assume a transversely isotropic distribution of asperities, we shall obtain a macroscopic elastic compliance that is also transversely isotropic. The analysis parallels that given above for asperity sintering.

4.1 Macro-micro relations We again assume affine deformation in order to connect macroscopic elastic straining to the local elastic deformation of asperities, and make use of the Principle of Virtual Work in order to calculate the macroscopic stress Σ_{ij} associated with any assumed macroscopic elastic strain E_{ij}. The following response is absent any contribution from sintering and Coble creep.

Recall the representative splat arrangement of Fig. 3. The local displacement between splats 0 and 1 across a side contact with outward normal $\boldsymbol{N}$ is related to the macroscopic elastic strain by

$$u_{\alpha}^{\mathrm{S}} = 2E_{\alpha\beta}N_{\beta}R \qquad (4.1)$$

where (α,β) are again in the range (1,2). Similarly, the relative displacement between splats 0 and 2, across the top face is

$$u_i^{\mathrm{T}} = E_{i\beta} N_\beta R + 2E_{i3} h \tag{4.2}$$

The inter-splat normal displacement u_N^{S} gives rise to a normal asperity force f_N^{S} at each inter-splat asperity contact on the side-face of the representative splat 0. Similarly, the inter-splat displacement u_i^{T} on the top and bottom faces of splat 0 gives rise to an asperity force f_i^{T}. The Principle of Virtual Work then gives

$$\Sigma_{ij}\delta E_{ij} V = \frac{1}{2}\left[\int_{S^{\mathrm{T}}} m^{\mathrm{T}} f_i^{\mathrm{T}} \delta u_i^{\mathrm{T}} dS + \int_{S^{\mathrm{S}}} m^{\mathrm{S}} f_N^{\mathrm{S}} \delta u_N^{\mathrm{S}} dS \right] \tag{4.3}$$

where (f_N^{S}, f_i^{T}) are given in terms of ($u_N^{\mathrm{S}}, u_i^{\mathrm{T}}$) according to the contact stiffness of the asperities.

4.2 The contact stiffness of each asperity

We make use of the previous analysis by Fleck and Cocks (2009) in order to deduce the effective spring constant for the asperities, as follows. As for the sintering case, the asperities are assumed to slide freely, but possess a linear contact law in the normal direction.

We consider two extremes of topology for the asperities, regardless of whether the asperities are on the side faces or on the top and bottom of the splats. First, consider small, widely spaced asperities and treat them as isolated circular junctions of radius *b* and spacing ℓ bridging two parallel planes under a nominal tensile traction $T = mf$ where $m = 4/\left(\pi \ell^2\right)$ is the number of contacts per unit area, and f is the normal contact force carried by each junction. The associated displacement *u* is deduced from the solution for normal indentation of a half-space by a frictionless, rigid punch of circular section. The resulting contact stiffness k_1 is

$$k_1 = \frac{T}{u} = \frac{4bE'}{\pi \ell^2} \tag{4.4}$$

where $E' = E/\left(1-\nu^2\right)$. Now consider the other extreme topology where asperities bridge most of the nominal inter-splat contact area, with occasional spaces existing between the asperities. The normal contact stiffness is now (see Fleck and Cocks (2009) for details)

$$k_2 \equiv \frac{T}{u} = \frac{3\pi E'}{8d}\left[1-\frac{4b^2}{\ell^2}\right]^{-3/2} \tag{4.5}$$

In order to proceed, an interpolation formula is needed for the effective contact stiffness k between the values of k_1 at small b/ℓ and k_2 at b/ℓ close to 1/2. We make the choice

$$T = ku \tag{4.6}$$

where

$$k = \frac{k_1}{2}\left(1+\cos\frac{2\pi b}{\ell}\right)+\frac{k_2}{2}\left(1-\cos\frac{2\pi b}{\ell}\right) \tag{4.7}$$

as this preserves the asymptotic behaviour except for mid-range values of b/ℓ close to 1/4.

Now specialise to the case where the asperities are on the sides of the splats, and again employ a superscript S for asperities at the side of a splat. The traction follows directly from (4.6) as

$$T_\alpha^{\mathrm{S}} = k^{\mathrm{S}} N_\alpha N_\beta u_\beta^{\mathrm{S}} \tag{4.8a}$$

for $(\alpha,\beta)=(1,2)$ and

$$T_3^{\mathrm{S}} = 0 \tag{4.8b}$$

Here, k^{S} scales with b^{S} according to the prescription (4.7). The expression for the contact stiffness associated with contacting asperities on the top and bottom of the splats is made more complicated by the fact that these asperities are assumed to have a unit normal which is inclined randomly at an azimuthal angle ϕ between zero and ω, as detailed in section 2.1. Upon following the same procedure as that detailed in Appendix A, we obtain

$$T_\alpha^{\mathrm{T}} = k^{\mathrm{T}} u_\alpha^{\mathrm{T}} g_1(\omega) \tag{4.9}$$

for $\alpha=(1,2)$ and

$$T_3^{\mathrm{T}} = k^{\mathrm{T}} u_3^{\mathrm{T}} g_2(\omega) \tag{4.10}$$

As before, the superscript T indicates a quantity associated with the top (or bottom) surface of a splat and k^{T} is the contact stiffness for asperity tops and scales with b^{T} according to (4.7). The geometric parameters (g_1, g_2) have already been defined in (3.12).

We proceed by substituting (4.1), (4.2) and (4.8)-(4.10) into the Principle of Virtual Work, to obtain

$$\Sigma_{ij} = K_{ijkl} E_{kl} \tag{4.11}$$

where the macroscopic modulus K_{ijkl} arising from asperity stiffness is transversely isotropic, with components given explicitly in Appendix B. Note: for $\omega > 0$, full sintering of the asperities on the top and bottom of the splats results in both normal and sliding stiffnesses at the interface going to infinity. Elastic deformation of the asperities on the sides of the splats can then no-longer be accommodated by elastic sliding at the top and bottom faces. In this limit the macroscopic moduli in the x_1, x_2 and x_3 arising from asperity deformation all go to infinity, independent of the geometry of the asperities on the sides of the splats.

5. The overall macroscopic response due to inter-splat sintering, Coble creep of the splats and elasticity

The total strain rate $\dot{E}_{ij}$ has an elastic contribution $\dot{E}_{ij}^{\mathrm{EL}}$, a sintering contribution $\dot{E}_{ij}^{\mathrm{SIN}}$ and a Coble creep contribution $\dot{E}_{ij}^{\mathrm{C}}$ such that

$$\dot{E}_{ij} = \dot{E}_{ij}^{\mathrm{EL}} + \dot{E}_{ij}^{\mathrm{SIN}} + \dot{E}_{ij}^{\mathrm{C}} \tag{5.1}$$

Each contribution is related to the macroscopic stress (or its rate) as follows. The elastic contribution subdivides into a bulk contribution associated with elastic deformation of each splat $\dot{E}_{ij}^{\mathrm{B}}$ and the contribution $\dot{E}_{ij}^{\mathrm{A}}$ from asperity stiffness, such that $\dot{E}_{ij}^{\mathrm{EL}} = \dot{E}_{ij}^{\mathrm{A}} + \dot{E}_{ij}^{\mathrm{B}}$. For simplicity (and with little loss in accuracy) we introduce a bulk isotropic response, as characterised by a modulus E and a Poisson ratio ν, such that the bulk elastic strain rate is

$$\dot{E}_{ij}^{\mathrm{B}} = C_{ijkl}^{\mathrm{B}} \dot{\Sigma}_{kl} \tag{5.2a}$$

where the bulk compliance tensor reads

$$C_{ijkl}^{\mathrm{B}} = \frac{1+\nu}{2E}\left(\delta_{il}\delta_{jk} + \delta_{ik}\delta_{jl}\right) - \frac{\nu}{E}\delta_{ij}\delta_{kl} \tag{5.2b}$$

The elastic strain rate contribution from asperity stiffness follows immediately from (4.11) as

$$\dot{E}_{ij}^{\mathrm{A}} = K_{ijkl}^{-1} \dot{\Sigma}_{kl} \tag{5.3}$$

while the sintering contribution $\dot{E}_{ij}^{\mathrm{SIN}}$ follows immediately from (3.15). Finally, we consider the contribution from Coble creep of the splats. The columnar grain structure of the splats results in a transversely isotropic creep response such that

$$\dot{E}_{ij}^{\mathrm{C}} = \Pi_{ijkl} \Sigma_{kl} \tag{5.4}$$

where the components of Π_{ijkl} are given by Greenwood (1992), and are reproduced in Appendix B. Assembling the above relations gives the governing macroscopic constitutive relation,

$$\dot{E}_{ij} = \left(C_{ijkl}^{\mathrm{B}} + K_{ijkl}^{-1}\right)\ \dot{\Sigma}_{kl} + \Lambda_{ijkl}^{-1}\left(\Sigma_{kl} - \Sigma_{kl}^{\mathrm{SIN}}\right) + \Pi_{ijkl}\Sigma_{kl} \tag{5.5}$$

In summary, deformation of the TBC has four contributions:

(i) Elastic deformation of the splats (bricks), as characterised by a Young's modulus E and Poisson's ratio ν of the fully dense solid;

(ii) Elastic deformation of the asperities;

(iii) Coble creep of the splats; and

(iv) Diffusional growth of the asperity contact area, as characterised by the surface diffusivity D_{SIN} and grain-boundary diffusivity D_{G} , and driven by the contact pressure and the reduction in overall interface energy.

We need to combine eqn (5.5) with relationships for the time evolution of asperity geometry at the side and top of the splats, ie the rate of change of $(w^{\mathrm{S}}, b^{\mathrm{S}}, w^{\mathrm{T}}, b^{\mathrm{T}})$. The rates of change of w^{S} and w^{T} are determined in Appendix A and are given by

$$\dot{w}^{\mathrm{S}} = \Lambda_{\alpha\alpha kl}^{-1}\left(\Sigma_{kl} - \Sigma_{kl}^{\mathrm{SIN}}\right) R \tag{5.6}$$

and

$$\dot{w}^{\mathrm{T}} = \Lambda_{33kl}^{-1}\left(\Sigma_{kl} - \Sigma_{kl}^{\mathrm{SIN}}\right) 2hg_3(\omega) \tag{5.7}$$

Since the volume of the asperities is conserved during deformation, the contact radii evolve according to

$$\dot{b}^{\mathrm{S}} = \frac{b^{\mathrm{S}}\dot{w}^{\mathrm{S}}}{2w^{\mathrm{S}}} \qquad \text{and} \qquad \dot{b}^{\mathrm{T}} = \frac{b^{\mathrm{T}}\dot{w}^{\mathrm{T}}}{2w^{\mathrm{T}}} \qquad (5.8)$$

6. Sintering simulations and characteristic time scales

Equations (5-5) to (5.8) can be solved for any prescribed boundary value problem. Here we concentrate on the important practical problems of free and constrained sintering. Constrained sintering is representative of practical applications: the coating is bonded to a thick elastic substrate, and compatibility dictates that the in-plane strain within the coating equals that of the substrate. In contrast, when the coating is released from the substrate, it can sinter freely at temperature. The relative magnitude of free and constrained sintering responses can be measured experimentally and used (i) to calibrate the above constitutive model, and (ii) to determine the relative importance of Coble creep and interfacial diffusion upon the overall response.

In analysing each of these problems it is instructive to identify a number of characteristic timescales based upon a combination of constitutive and geometric properties of the coating. The sintering response depends upon the relative magnitude of these timescales and how they compare to the imposed sintering time at temperature. We proceed to analyse the characteristic timescales and we then make predictions of the free and constrained sintering responses in terms of these timescales.

6.1 Characteristic time scales for free sintering

Since free sintering is stress-free, it involves neither Coble creep of the splats nor elastic deformation of the asperities and splats. The sintering response and evolution of macroscopic properties, such as the elastic moduli and thermal conductivities in the coating are determined by asperity-diffusion between the splats. We can identify two characteristic timescales for these processes. These are:

(i) *The characteristic time τ_1 for free sintering of the asperities on the sides of the splats*. This timescale is obtained by integration of (3.6) between the limits of the

initial asperity height $w^{S} = w_0^{S}$ and $w^{S} = 0$. Upon taking *f*=0 (for free sintering), and assuming that the asperity geometry is of the form *b>>w*, integration gives

$$\tau_1 = \frac{\left(w_0^{S} b_0^{S}\right)^2}{8D_{G}\left(2\gamma_{SUR} - \gamma_{G}\right)} \tag{6.1}$$

We shall make extensive use of τ_1 as the reference timescale for both free and constrained sintering, and use it to normalise the sintering time in the full numerical simulations below.

(ii) *The characteristic time* τ_2 *for free sintering of the asperities on the top and bottom of a splat*. Upon integrating (3.11) between $w^{T} = w_0^{T}$ and $w^{T} = 0$ under condition of free sintering, the resulting timescale is

$$\tau_2 = \frac{\left(w_0^{T} b_0^{T}\right)^2 g_2(\omega)}{8D_{G}\left(2\gamma_{SUR} - \gamma_{G}\right) g_3(\omega)} \approx \frac{\left(w_0^{T} b_0^{T}\right)^2}{8D_{G}\left(2\gamma_{SUR} - \gamma_{G}\right)} \tag{6.2}$$

for small ω.

In free sintering, the sintering response at the top and bottom of the splats is independent of that at the sides of the splats when $\omega = 0$, and the relative rate is given by the ratio of time scales τ_2 / τ_1, where

$$\frac{\tau_2}{\tau_1} = \left(\frac{w_0^{T} b_0^{T}}{w_0^{S} b_0^{S}}\right)^2 \tag{6.3}$$

This ratio is simply a function of relative asperity geometry at the top and side of a splat and involves no kinetic parameters.

6.2 Characteristic time scales for constrained sintering

Next, consider the situation where a coating is attached to a substrate. In most practical cases, the substrate is much thicker than that of the coating, and consequently the equi-biaxial, in-plane strain state within the coating matches that of the substrate. An equi-biaxial, in-plane stress within the coating arises initially from thermal expansion mismatch between coating and substrate, and evolves as a result of Coble creep and asperity sintering of the coating.

Consider the isothermal case where the temperature of the coating and substrate are suddenly changed. An in-plane stress is generated in the coating as a result of the thermal expansion mismatch between coating and substrate. Subsequently, this stress relaxes as a result of Coble creep of the splats and/or sintering of the asperities, towards a steady state stress as determined by the sintering stress of (3.14). A number of additional timescales now need to be considered.

(i) *The characteristic time τ_3 for pressure-assisted asperity sintering.* Consider an APS layer under an in-plane equi-biaxial pressure *p*. Neglect the contributions to in-plane strain from Coble creep and elasticity, and assume that the local sintering force on the sides of the asperities is given by

$$f^{\mathrm{S}} = \frac{\pi\left(\ell^{\mathrm{S}}\right)^2 p}{4} >> f^{\mathrm{S}}_{\mathrm{SIN}} \tag{6.4}$$

Integration of (3.6) between the limits of the initial asperity height $w^{\mathrm{S}} = w^{\mathrm{S}}_0$ and $w^{\mathrm{S}} = 0$ gives a macroscopic sintering strain of $w^{\mathrm{S}}_0 / 2R$ and a sintering time

$$\tau_3 = \frac{w^{\mathrm{S}}_0 \left(b^{\mathrm{S}}_0\right)^4}{2D_{\mathrm{G}}\left(\ell^{\mathrm{S}}\right)^2 p} \tag{6.5}$$

where b^{S}_0 is the initial radius of the asperity. This result has been obtained under the usual assumption that $D_{\mathrm{G}} << D_{\mathrm{SUR}}$ and noting that *w*<<*b* in (3.7). Consequently, the asperity viscosity (3.7) is dominated by the contribution from the contact between asperities (that is, the first term on the r.h.s. of (3.7)).

(ii) *The characteristic time τ_4 for pressure-assisted Coble creep.* This is the time required to generate a creep strain (under an in-plane pressure *p*) of $w^{\mathrm{S}}_0 / 2R$. The characteristic time follows from (5.4) as

$$\tau_4 = \frac{\alpha h^3 w^{\mathrm{S}}_0}{3RD_{\mathrm{G}} p} \tag{6.6}$$

The ratio τ_4 / τ_3 is given by

$$\frac{\tau_4}{\tau_3} = \frac{2\alpha h^3 \left(\ell^{\mathrm{S}}\right)^2}{3R\left(b_0^{\mathrm{S}}\right)^4} \tag{6.7}$$

If this ratio is small, relaxation of stress in the coating is driven by Coble creep. Conversely, if it is large, then asperity sintering dominates.

(iii) *The characteristic time τ_5 for stress relaxation by Coble creep*. Consider the case where Coble creep is much faster than asperity sintering ($\tau_4 / \tau_3 << 1$). Upon subjecting the coating and substrate to a sudden jump in temperature an initial in-plane equi-biaxial stress, $\Sigma_{11} = \Sigma_{22} = \Sigma_0$, is generated in the coating. This stress relaxes in accordance with (5.5), with $\dot{E}_{11} = \dot{E}_{22} = 0$. Since the in-plane modulus of APS coatings are much less than that of the fully dense solid, we infer that the asperity compliance K_{ijkl}^{-1} much exceeds the bulk compliance C_{ijkl}^{B} and (5.5) simplifies to

$$\tau_5 \dot{\Sigma}_{11} + \Sigma_{11} = 0 \tag{6.8}$$

where

$$\tau_5 = \left(K_{1111} + K_{1122}\right)^{-1} \left(\Pi_{1111} + \Pi_{1122}\right)^{-1} \tag{6.9}$$

This equation simplifies to

$$\tau_5 = \frac{\alpha h^3}{3k^{\mathrm{S}} R D_{\mathrm{G}}} \tag{6.10}$$

for the case where the waviness ω at the top and bottom of the splats is negligible. It is clear from (5.11) that the relaxation time is very sensitive to the splat height *h*; it also depends upon the diameter-to-height aspect ratio α of the columnar grains within each splat and upon the asperity geometry via the k^{S} term.

(iv) *The characteristic time τ_6 for stress relaxation by asperity sintering*. Now consider the case where asperity sintering is much faster than Coble creep ($\tau_4 / \tau_3 >> 1$). Then, upon modifying the above analysis for τ_5 the relaxation time becomes

$$\tau_6 = \frac{\tau_3 \tau_5}{\tau_4} = \frac{\left(b_0^{\mathrm{S}}\right)^2}{16 k^{\mathrm{S}} D_{\mathrm{G}}} \tag{6.11}$$

It is instructive to compare the stress relaxation time τ_6 with the sintering time for the constrained coating. We shall show below by full numerical simulation that the sintering time scales with the free sintering time τ_1. The ratio τ_6 / τ_1 is on the order of the elastic strain in the asperities due to a local sintering stress of magnitude $\left(2\gamma_{\mathrm{SUR}} - \gamma_{\mathrm{G}}\right) / w_0^{\mathrm{S}}$ and this strain level is always much less than unity. Consequently, the time for stress relaxation within the coating is much less than the full sintering time of the constrained coating. This conclusion also holds when Coble creep dominates the stress relaxation event; then, the relaxation time is τ_5, and this is much less than τ_6. Thus, stress relaxation is always much faster than sintering of the constrained coating.

7. Simulations of sintering and property evolution

In this section we consider the sintering of free-standing and constrained APS coatings and how the sintering process influences the evolution of elastic properties. Consider the problem of heating the APS ceramic layer (and substrate in the case of constrained sintering) to a sufficiently high temperature (say 1000^{o}C) that the ceramic undergoes bulk creep and sintering. We shall assume, unless otherwise stated, the following geometric values and material properties, consistent with those used by Cocks and Fleck (2010) in their previous study on the sintering of YSZ-based APS coatings: E=170 GPa, ν=0.3, γ_{SUR}=1 Jm^{-2}, γ_G=0.64 Jm^{-2}, D_{SUR}=6.0x10^{-31} m^{6}J^{-1}s^{-1}, D_{G}=6.0x10^{-31} m^{6}J^{-1}s^{-1}, b^{S}=0.5 μm, w^{S}=0.5 μm, ℓ^{S}=10 μm, b^{T}=0.5 μm, w^{T}=0.5 μm, ℓ^{T}=10 μm, R=25 μm, h=1.0 μm, and $\alpha = d / h = 0.1$. However, results will be plotted in non-dimensional form. All simulations are performed using a 4$^{\mathrm{th}}$ order Runge-Kutta procedure to integrate (5.5)-(5.7) forward in time.

7.1 Free sintering of coating

Consider first the case of free sintering of a TBS layer. The macroscopic stress vanishes, $\Sigma_{ij} = 0$, and the strain rate $\dot{E}_{ij}$ is driven by the sintering stress $\Sigma_{ij}^{\mathrm{SIN}}$ in accordance with (3.13). The evolution of strain components $\left(E_{11}, E_{33}\right)$, normalised asperity radius $\left(b^{\mathrm{S}} / \ell^{\mathrm{S}}, b^{\mathrm{T}} / \ell^{\mathrm{S}}\right)$ and normalised moduli $\left(E_1/E, E_3/E\right)$ are plotted as a function of t/τ_1 in Fig. 5a,b and c, respectively. These results assume that asperities

on the top face of the splats are orientated along the face normal, $\omega = 0$; the equivalent set of plots, for inclined asperities with $\omega = 20^{o}$ are given in Fig. 6a-c. In each plot of Figs. 5 and 6, three cases are considered: (i) the baseline reference case, where the asperity geometry at the top and side of the splats are identical, implying that $\tau_2/\tau_1 = 1$ from (6.3); (ii) the top asperities have twice the linear dimensions and spacing of the side asperities, implying $\tau_2/\tau_1 = 16$; and (iii) the top asperities have half the linear dimensions and spacing of the side asperities, implying $\tau_2/\tau_1 = 1/16$.

Consider the strain evolution for $\omega = 0$, as reported in Fig. 5a. It is striking that both strain components increase linearly with time. This can be explained by considering the analytical expressions for strain rate, and upon taking the dominant terms. Making use of (B.1) the governing relation (3.13) reduces to:

$$\dot{E}_{11} = -\frac{f_{\mathrm{SIN}}^{\mathrm{S}}}{2\lambda^{\mathrm{S}} R} \approx -\frac{4\left(2\gamma_{\mathrm{SUR}} - \gamma_{\mathrm{G}}\right) D_{\mathrm{G}}}{R w^{\mathrm{S}} \left(b^{\mathrm{S}}\right)^2} \tag{7.1}$$

and

$$\dot{E}_{33} = -\frac{f_{\mathrm{SIN}}^{\mathrm{T}}}{2\lambda^{\mathrm{T}} h} \approx -\frac{4\left(2\gamma_{\mathrm{SUR}} - \gamma_{\mathrm{G}}\right) D_{\mathrm{G}}}{h w^{\mathrm{T}} \left(b^{\mathrm{T}}\right)^2} \tag{7.2}$$

Recall that the volume of an asperity is taken to be constant; consequently, $w^{\mathrm{S}}\left(b^{\mathrm{S}}\right)^2$ in (7.1) and $w^{\mathrm{T}}\left(b^{\mathrm{T}}\right)^2$ in (7.2) do not evolve with time, and the strain rates are constant. Further, it is clear from (7.1) and (7.2) that the in-plane and out-of-plane responses are independent.

Free sintering on the sides of the splats dictates the evolution of in-plane strain E_{11} and modulus E_1, and runs to completion ($b^{\mathrm{S}} \to 0.5\ell^{\mathrm{S}}$) over a timescale of τ_1. Likewise, free sintering on the tops of the splats dictates the evolution of out-of-plane strain E_{33} and modulus E_3, and occurs over a timescale of τ_2. As the asperities grow in diameter (see Fig. 5b), the strain $\left(E_{11}, E_{33}\right)$ and moduli $\left(E_1/E, E_3/E\right)$ increase accordingly. Since the kinetic processes driving diffusion at the sides and tops of the splats are the same, the only difference in responses at the top and sides is due to

differences in asperity geometry and splat aspect ratio. For example, the high aspect ratio h/R of the splats leads to a much larger sintering strain in the through-thickness direction (in the range of -0.1 to -0.5) than in the in-plane direction (on the order of -0.01).

The asperity radii $\left(b^{\mathrm{S}}, b^{\mathrm{T}}\right)$, and consequently the in-plane and out-of-plane moduli, increase rapidly towards the end of the sintering period, see Figs. 5b and 5c, respectively. The initial moduli are also sensitive to the aspect ratio h/R of the splats: there is a much greater density of the compliant inter-splat interfaces in the out-of-plane x_3 direction than in the x_1 in-plane direction.

Second, consider the case $\omega = 20^{\mathrm{o}}$, as reported in Fig. 6. The relative sliding at the top (and bottom) of splats now entails sintering of asperities at the top (and bottom) of the splats, and this restricts the rate of sintering in the in-plane direction. To make this statement quantitative, make use of (B.1) in order to reduce the governing relation (3.13) to:

$$\dot{E}_{11} = -\left(2\lambda^{\mathrm{S}} m^{\mathrm{S}} R + \frac{0.0594 \lambda^{\mathrm{T}} m^{\mathrm{T}} R^2}{h} \right)^{-1} m^{\mathrm{S}} f_{\mathrm{SIN}}^{\mathrm{S}} \qquad (7.3)$$

and

$$\dot{E}_{33} = -\frac{-0.671}{\lambda^{\mathrm{T}} h} f_{\mathrm{SIN}}^{\mathrm{T}} \qquad (7.4)$$

The term in parenthesis on the r.h.s. of (7.3) now contains a contribution from the top of the asperities and thereby retards the sintering rate in the in-plane direction. Initially, this term is small and the macroscopic strain rate in (7.3) is close to that in (7.1), and is almost constant. However, when the asperities on the top of the splats sinter to full density before those on the sides, this term becomes large and sintering of the side asperities become heavily constrained. Sliding at the top of splats now requires diffusion over the length scale of the sintered asperities at the top and bottom of the splats.

The above argument is borne out by the calculations shown in Fig. 6. The constrained response differs substantially from the free sintering behaviour of Fig. 5 only for

$\tau_2 < \tau_1$. In this regime, the top of a splat sinters before its sides; once the top has sintered, any subsequent in-plane sintering is retarded.

It is further noted from Fig. 6c that the choice $\omega = 20^o$ leads to a slight elevation in the in-plane modulus prior to full sintering at the top of a splat (at $t < \tau_2$). This is traced to the feature that macroscopic in-plane elastic straining requires deformation of the angular asperities on the top face of a splat in addition to deformation on the side face. When the top face of a splat has fully sintered (at $t > \tau_2$), the splats have inter-locked elastically and $E_3 = E$. In this limit, the splat boundaries with discrete asperities no longer form an interconnected network throughout the coating. The side faces now behave as cracks within a continuous matrix bridged by asperities as assumed in the *stage II* sintering model described by Fleck and Cocks (2009). In practice there will be a gradual transition from *stage I* to *stage II* behaviour. We leave further consideration of this to a later paper.

7.2 Constrained sintering of coating

When an APS coating and its substrate are subjected to a step change in temperature, the coating instantaneously responds thermo-elastically and acquires a jump in in-plane stress. This stress relaxes rapidly over a period on the order of τ_5 or τ_6, as discussed in section 6.2. The subsequent response is by a combination of Coble creep and asperity sintering, with elastic strain rates dominated by the rates due to these processes. Again, take the Cartesian axes x_1 and x_2 to lay in the plane of the coating. Then, for this subsequent response, (5.5) reduces to

$$\dot{E}_{11} = \dot{E}_{22} = A\left(\Sigma_{11} - \Sigma_{11}^{\mathrm{SIN}}\right) + B\Sigma_{11} = 0 \qquad (7.5)$$

where $A = \left(\Lambda_{1111}^{-1} + \Lambda_{1122}^{-1}\right)$, $B = \left(\Pi_{1111} + \Pi_{1122}\right) = 3D_{\mathrm{G}} / \left(2\alpha h^3\right)$ and $\Sigma_{11}^{\mathrm{SIN}}$ is given by eqn (3.14). Suitable rearrangement of (7.1) gives

$$\Sigma_{11} = \frac{A}{A+B}\Sigma_{11}^{\mathrm{SIN}} \qquad (7.6)$$

The rate of change of height of the asperities on the sides of the splats, (5.5) is then given by

$$\dot{w}^{\mathrm{S}} = 2A\left(\Sigma_{11} - \Sigma_{11}^{\mathrm{SIN}}\right)R = \frac{2AB}{A+B}\Sigma_{11}^{\mathrm{SIN}}R \qquad (7.7)$$

Integrating this between the limits $w^{\mathrm{S}} = w_0^{\mathrm{S}}$ and $w^{\mathrm{S}} = 0$ gives the time for sintering of asperities as

$$\tau_{\mathrm{CON}} \approx \tau_1 \left(1 + \frac{1}{3} \frac{\tau_4}{\tau_3} \right) \tag{7.8}$$

Upon recalling that the time for free sintering approximately equals τ_1, we conclude that constrained sintering takes longer than free sintering by about $\tau_1 \tau_4 / (3\tau_3)$.

The constrained sintering response, $\left(b^{\mathrm{S}} / \ell^{\mathrm{S}}, b^{\mathrm{T}} / \ell^{\mathrm{S}} \right)$ versus time, is shown in Fig. 7 for the same set of parameters as that employed in Fig. 5, again with $\omega = 0$. The three cases shown in Fig. 7 are: (i) the baseline reference case, where the asperity geometry at the top and side of the splats are identical, implying that $\tau_2 / \tau_1 = 1$; (ii) the top asperities have twice the linear dimensions and spacing of the side asperities, implying $\tau_2 / \tau_1 = 16$; and (iii) the top asperities have half the linear dimensions and spacing of the side asperities, implying $\tau_2 / \tau_1 = 1/16$. In all three cases, the ratio τ_4 / τ_3 equals 4.26, and consequently stress relaxation within the coating is by a combination of Coble creep and asperity sintering. The *in-plane* sintering rate is slower than that of free sintering by a factor of about 2.4, recall (7.10). In contrast, the sintering rate in the *out-of-plane* direction is the same as that for free sintering.

The effect of the size of the asperities on the sides of the splats upon sintering rate is explored in Fig. 8. Two cases are considered: the reference case, and the choice where the size of all geometric features associates with side asperities and top asperities is increased by a factor of x10. The corresponding values of τ_4 / τ_3 are 4.26 and 426. A value of τ_4 / τ_3 =426 implies that the Coble creep rate is much less than that of sintering; since the in-plane sintering strain equals that of the substrate, this implies that Coble creep constrains the rate of sintering, and so the rate of asperity sintering at the sides of the splats is reduced compared to the case of τ_4 / τ_3 =4.26, see Fig. 8a. The increased resistance to Coble creep also leads to an increase in the in-plane stress, see Fig. 8b. Now consider sintering in the out-of-plane direction. There is no interaction between the in-plane and out-of-plane sintering responses when $\omega = 0$, and

so the rate of out-of-plane sintering in Fig. 8a is the same for τ_4/τ_3 equal to 4.26 and 426.

Finally, we consider constrained sintering for inclined top asperities, $\omega = 20^o$, see Fig. 9. Two choices of asperity size are again assumed such that τ_4/τ_3 equals 4.26 and 426. The larger value of τ_4/τ_3, associated with larger asperities, again retards the rate of Coble creep in relation to sintering, and so the overall sintering rate is reduced, see Fig. 9a. Also, the inclined asperities on the tops of splats restricts the relative sliding of the top of splats, and this retards the rate of in-plane sintering compared to the case $\omega = 0$ as depicted in Fig. 8a. This is a major effect for the choice τ_4/τ_3 =4.26: the in-plane sintering time is increased by two orders of magnitude when ω is increased from zero to 20^o. Sintering at the top of the splats also has a controlling effect upon both in-plane and out-of-plane moduli, see Fig. 9b. After a time $t = \tau_1 = \tau_2$, the top of the splats have fully sintered and $E_1 = E_3 = E$. As discussed at the end of section 7.2, in practice there will be a transition from stage I to stage II sintering behaviour as the top asperities fully sinter.

8. Concluding remarks

The present study has highlighted the role played by microstructural feature of APS coatings over a very wide range of length scales, from nano-scale features to splat dimensions. It is remarkable that the complex geometrical features and kinetic parameters are subsumed into a relatively short list of characteristic time-scales. The ratio of these time-scales dictates the relative role played by diffusional flow, Coble creep and elastic deformation. The study has highlighted the role of asperity shape and inclination, and the degree of cross-coupling between in-plane and out-of-plane behaviour for both free and constrained sintering.

The brick model is a fully-developed constitutive description with physically motivated internal state variables. As such, it is suitable for implementation in implicit and explicit finite element codes. Here, we have limited attention to simple, but practically relevant, stress states that can be solved by time integration of a limited set of non-linear rate equations. Experiments are required in order to assess the accuracy of current predictions, such as the evolution of microstructure and elastic properties in

both free and constrained sintering. Some data of this type already exists in the literature. For example, Thompson and Clyne (2001) have measured the sintering response of a free standing coating and of a coating constrained by a substrate. The constraint led to a slower rate of increase of modulus compared with the free sintering case.

It is recognised that the performance and durability of an APS TBC is closely linked to the out-of-plane thermal conductivity and the in-plane modulus. The current model makes predictions of the in-plane and out-of-plane moduli, but we leave to a subsequent study the prediction of in-plane and out-of-plane thermal conductivities.

References

Ashby, M.F. (1974). A first report on sintering diagrams. *Acta Metall.*, **22**(3), 275-289.

Cernuschi F, Bison PG, Marinetti S, Scardi P. (2008). Thermophysical, mechanical and microstructural characterization of aged free-standing plasma-sprayed zirconia coatings *Acta Materialia*, **56**, 4477-4488.

Cipitria A, Golosnoy IO, Clyne TW. (2009a). A sintering model for plasma-sprayed zirconia TBCs. Part I: Free-standing coatings. *Acta Materialia*, **57**, 980-992.

Cipitria A, Golosnoy IO, Clyne TW. (2009b). A sintering model for plasma-sprayed zirconia thermal barrier coatings. Part II: Coatings bonded to a rigid substrate. *Acta Materialia*, **57**, 993-1003.

Cocks, A.C.F. and Fleck, N.A. (2010). Constrained sintering of an air-plasma sprayed thermal barrier coating. *Acta Materialia*, **58**, 4233-4244.

Coble, R.L. (1963). A model for boundary diffusion controlled creep in polycrystalline materials. *J. Appl. Phys.*, **34**, 1679-1682.

Erikkson, R., Brodin, H., Johansson, S., Ostergren, L. and Li, X-H. (2012). Fractographic and microstructural study of isothermally and cyclically heat treated thermal barrier coatings. *Surface and Coatings Technology*, in press, doi:10.1016/j.surfcoat.2012.02.040

Fleck, N.A. and Cocks, A.C.F (2009). A multiscale constitutive model for the sintering of an air-plasma prayed thermal barrier coating, and its response under hot isostatic pressing. *J. Mech. Phys. Solids*, **57**, 689–705.

Greenwood, G.W. (1992). A formulation for anisotropy in diffusional creep. *Proc. Roy Soc. Lond. Series A*, **436**, 187-196.

Sevostianov, I., Kachanov, M., Ruud, J., Lorraine, P. and Dubois, M. (2004). *Mat Sci and Engineering*, **A386**, 164-174.

Takagi, K., Kudo, D., Kawasaki, A. and Harada, Y. (2011). Microstructural dependency of thermal expansion and sintering shrinkage in plasma-sprayed zirconia coatings. *Surface and Coatings Technology*, **205**, 4411-417.

Thompson, J.A. and Clyne, T.W. (2001). The effect of heat treatment on the stiffness of zirconia top coats in plasma-sprayed TBCs**,** *Acta Materialia*, **49**, 1565-1575.

Appendix A. Contact law for asperities on the top and bottom faces of a splat

Recall that the contact law relating the normal force f on an asperity to the normal separation rate $\dot{w}$ is given by (3.6). Now assume that the asperities on the top and bottom faces of a splat possess randomly orientated asperities with unit normal $\boldsymbol{n}$ as shown in Figs. 3 and 4a. The orientation of $\boldsymbol{n}$ is given by (2.2) and the spherical co-ordinates (ϕ,ψ) range over $0 \le \phi \le \omega$ and $0 \le \psi \le 2\pi$. Assume that all orientations within this domain are equally likely. Then, upon writing the relative velocity of a splat and its top-neighbour as $\dot{u}_i^{\mathrm{T}}$, the normal velocity at a representative asperity is

$$\dot{w}^{\mathrm{T}} = n_i \dot{u}_i^{\mathrm{T}} \tag{A.1}$$

A virtual work statement is used to relate the AVERAGE asperity force f_i^{T} to $\dot{u}_i^{\mathrm{T}}$:

$$f_i^{\mathrm{T}} \delta\dot{u}_i^{\mathrm{T}} = \frac{1}{\Omega}\int_0^{2\pi} d\psi \int_0^{\omega} d\phi \sin\phi \left[f n_i \delta\dot{u}_i^{\mathrm{T}} \right] \tag{A.2}$$

where

$$f^{\mathrm{T}} = \lambda^{\mathrm{T}} n_i \dot{u}_i^{\mathrm{T}} + f_{\mathrm{SIN}}^{\mathrm{T}} \tag{A.3}$$

and

$$\Omega = \int_0^{2\pi} d\psi \int_0^{\omega} d\phi \sin\phi = 2\pi\left(1-\cos\omega\right) \tag{A.4}$$

Direct evaluation of (A.2) gives (3.10) and (3.11) for the average asperity force on the top (or bottom) of a splat.

Appendix B. The viscosity tensor $\boldsymbol{\Lambda}$ and the stiffness tensor $\boldsymbol{K}$

The viscosity tensor for asperity sintering
The transversely isotropic viscosity tensor $\boldsymbol{\Lambda}$ arises from sintering of the asperities, and has the following non-vanishing components:

$$\begin{aligned}
\Lambda_{1111} &= \Lambda_{2222} = \frac{3\lambda^{\mathrm{S}} m^{\mathrm{S}} R}{2} + \frac{\lambda^{\mathrm{T}} m^{\mathrm{T}} R^2}{4h} g_1(\omega) \\
\Lambda_{3333} &= 2\lambda^{\mathrm{T}} m^{\mathrm{T}} h g_2(\omega) \\
\Lambda_{1122} &= \Lambda_{2211} = \frac{\lambda^{\mathrm{S}} m^{\mathrm{S}} R}{2} \\
\Lambda_{2323} &= \Lambda_{1313} = \frac{\lambda^{\mathrm{T}} m^{\mathrm{T}} h}{2} g_1(\omega) + \frac{\lambda^{\mathrm{T}} m^{\mathrm{T}} R^2}{16h} g_2(\omega)
\end{aligned} \tag{B.1}$$

along with the symmetries

$$\begin{aligned}
\Lambda_{1212} &= \frac{1}{2}\left(\Lambda_{1111} - \Lambda_{1122}\right) \\
\Lambda_{1212} &= \Lambda_{2121} = \Lambda_{1221} = \Lambda_{2112} \\
\Lambda_{2323} &= \Lambda_{3232} = \Lambda_{2332} = \Lambda_{3223}
\end{aligned}$$

and

$$\Lambda_{1313} = \Lambda_{3131} = \Lambda_{1331} = \Lambda_{3113} \tag{B.2}$$

We emphasise that the above brick model predicts no interaction between the in-plane and out-of-plane directions, implying that $\Lambda_{1133} = \Lambda_{3311} = \Lambda_{2233} = \Lambda_{3322} = 0$.

The stiffness tensor for elastic deformation of asperities
The transversely isotropic stiffness tensor $\boldsymbol{K}$ is due to the contact stiffness of asperities, and has the following non-vanishing components:

$$\begin{aligned}
K_{1111} &= K_{2222} = \frac{3k^{\mathrm{S}} R}{2} + \frac{k^{\mathrm{T}} R^2}{4h} g_1(\omega) \\
K_{3333} &= 2k^{\mathrm{T}} h g_2(\omega) \\
K_{1122} &= K_{2211} = \frac{k^{\mathrm{S}} R}{2} \\
K_{1212} &= \frac{1}{2}\left(K_{1111} - K_{1122}\right) \\
K_{2323} &= K_{1313} = \frac{k^{\mathrm{T}} h}{2} g_1(\omega) + \frac{k^{\mathrm{T}} R^2}{16h} g_2(\omega)
\end{aligned} \tag{B.3}$$

along with the symmetries

$$\begin{aligned}
K_{1212} &= K_{2121} = K_{1221} = K_{2112} \\
K_{2323} &= K_{3232} = K_{2332} = K_{3223}
\end{aligned}$$

and

$$K_{1313} = K_{3131} = K_{1331} = K_{3113} \tag{B.4}$$

Again, there is no coupling between the in-plane and out-of-plane directions, such that $K_{1133} = K_{2233} = 0$.

The Coble Creep Tensor

Greenwood (1992) has determined the Coble creep response for aligned, ellipsoidal grains. We shall idealise the columnar grains within each splat as oblate spheroids, with major axis equal to the splat height 2*h* and aligned with the $\boldsymbol{e}_3$ axis of Fig. 3, and with minor axis *d*. Define the aspect ratio of the grains by $\alpha = d / 2h$ and take $\alpha << 1$. In this limit, the Greenwood (1992) formulae read

$$\Pi_{1111} = \Pi_{2222} = \frac{3\left(1+\alpha^2\right)D_{\mathrm{G}}}{2\alpha^3 h^3}$$

$$\Pi_{1122} = \Pi_{2211} = \frac{-3D_{\mathrm{G}}}{2\alpha^3 h^3}$$

$$\Pi_{1212} = \frac{1}{2}\left(\Pi_{1111} - \Pi_{1122}\right)$$

$$\Pi_{1133} = \Pi_{3311} = \frac{-3D_{\mathrm{G}}}{2\alpha h^3}$$

$$\Pi_{3333} = \frac{3D_{\mathrm{G}}}{\alpha h^3}$$

$$\Pi_{2323} = \Pi_{1313} = \frac{3D_{\mathrm{G}}}{\alpha h^3} \tag{B.5}$$

along with the symmetries

$$\Pi_{2233} = \Pi_{3322} = \Pi_{1133} = \Pi_{3311}$$

$$\Pi_{1212} = \Pi_{2121} = \Pi_{1221} = \Pi_{2112}$$

$$\Pi_{2323} = \Pi_{3232} = \Pi_{2332} = \Pi_{3223}$$

and

$$\Pi_{1313} = \Pi_{3131} = \Pi_{1331} = \Pi_{3113} \tag{B.6}$$

All other components are zero. For the case of Coble creep, the terms $\Pi_{2233} = \Pi_{3322} = \Pi_{1133} = \Pi_{3311}$ are non-zero. Thus, cross-coupling exists between the in-plane and out-of-plane directions.

Figure Captions

Fig 1. Main features of the APS coating

Fig 2. A hexagonal arrangement of layered splats

Fig 3. Idealisation of 3 neighbouring splats.

Fig 4. Orientation of asperities at (a) top and bottom of splat, and (b) side of splat.

Fig 5. Free sintering of an APS coating for $\omega = 0$. The numbers on the plots correspond to the values of τ_2 / τ_1 used in the simulations. (a) In-plane, E_{11} (continuous lines) and out-of-plane, E_{33} (dashed lines) strains. (b) Normalised asperity radii on the sides (continuous line) and tops (dashed lines) of the splats. (c) Normalised in-plane, E_1 (continuous line) and out-of-plane, E_3 (dashed lines) moduli.

Fig 6. Free sintering of an APS coating for $\omega = 20^{\mathrm{o}}$. The numbers on the plots correspond to the value of τ_2 / τ_1 used in the simulation. (a) In-plane, E_{11} (continuous lines) and out-of-plane, E_{33} (dashed lines) strains. (b) Normalised asperity radii on the sides (continuous line) and tops (dashed lines) of the splats. (c) Normalised in-plane, E_1 (continuous line) and out-of-plane, E_3 (dashed lines) moduli.

Fig 7. The influence of τ_2 / τ_1 on the constrained sintering of an APS coating for $\omega = 0$ and $\tau_4 / \tau_3 = 4.26$. The continuous line represents the evolution of $b^{\mathrm{S}} / \ell^{\mathrm{S}}$ and the dashed lines the evolution of $b^{\mathrm{T}} / \ell^{\mathrm{S}}$.

Fig 8. The influence of τ_4 / τ_3 on the constrained sintering of an APS coating for $\omega = 0$. (a) Normalised asperity radii on the sides (continuous line) and tops (dashed lines) of the splats. (b) Normalised in-plane stress.

Fig 9. The influence of τ_4 / τ_3 on the constrained sintering of an APS coating for $\omega = 20^{\mathrm{o}}$. (a) Normalised asperity radii on the sides (continuous lines) and tops (dashed line) of the splats. (b) Normalised in-plane, E_1 (continuous lines) and out-of-plane, E_3 (dashed lines) moduli.

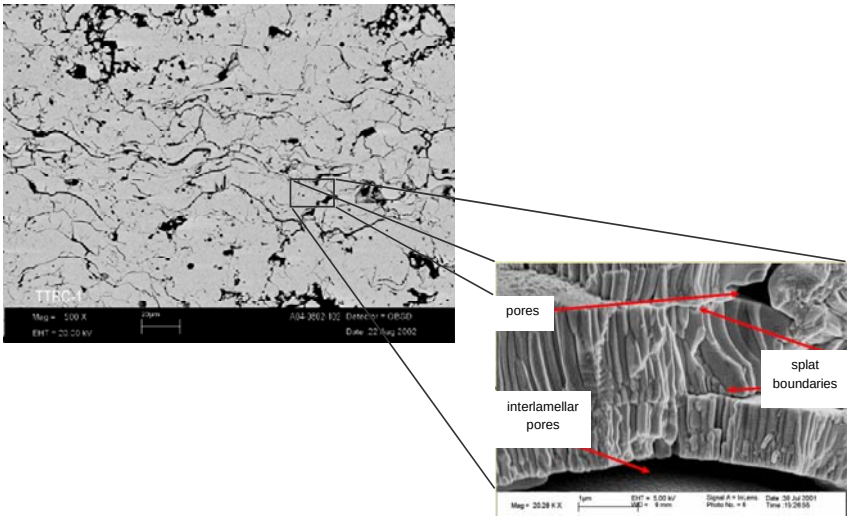

Fig 1. Main features of the APS coating

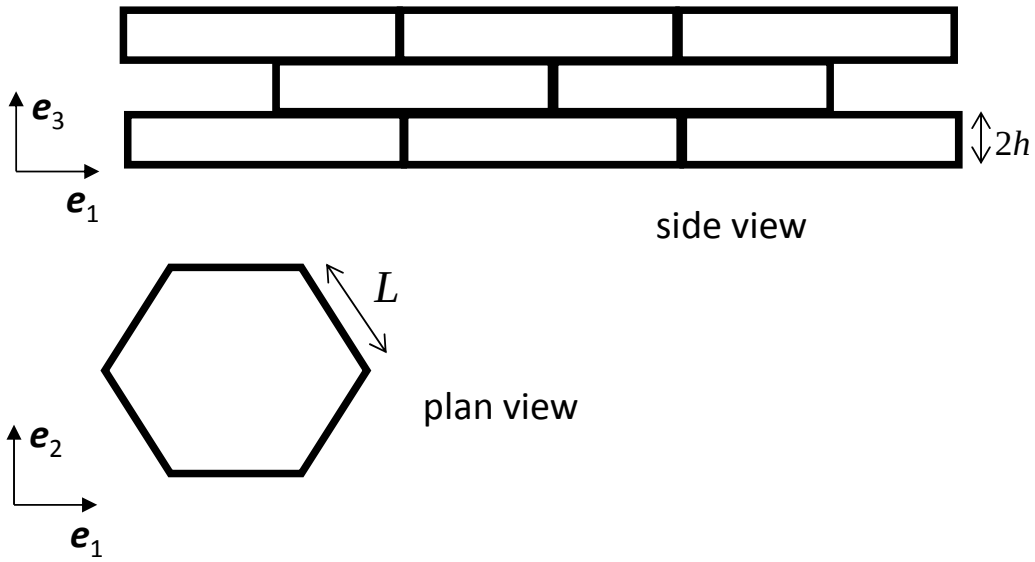

Fig 2. A hexagonal arrangement of layered splats

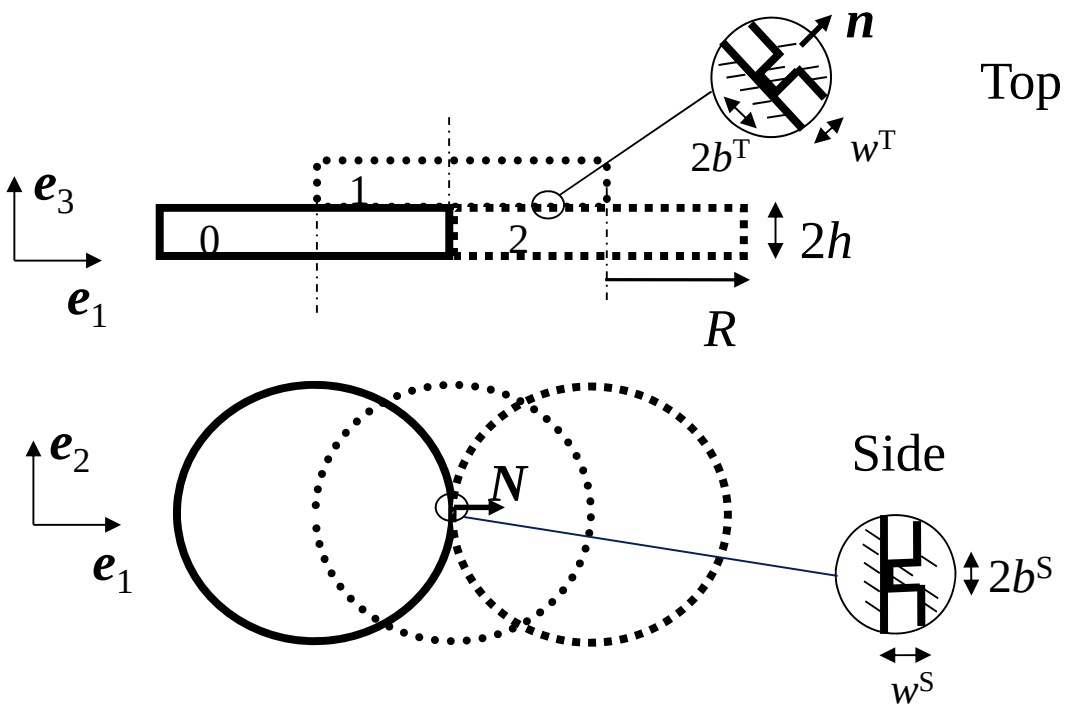

Fig 3. Idealisation of 3 neighbouring splats.

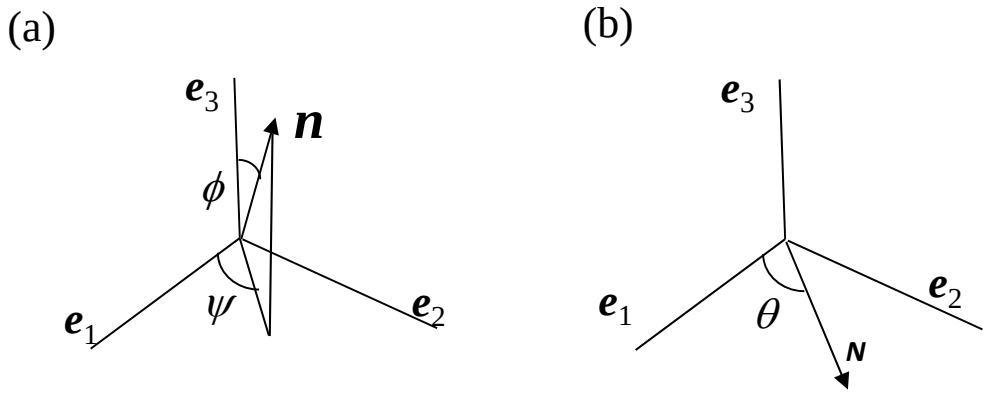

Fig 4. Orientation of asperities at (a) top and bottom of splat, and (b) side of splat.

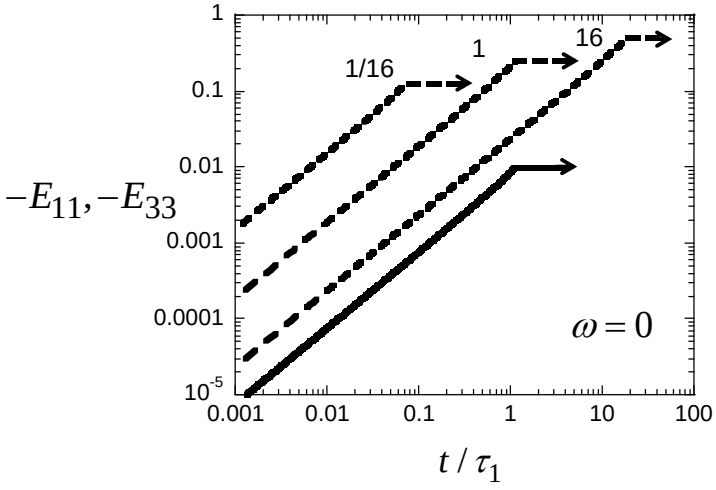

(a)

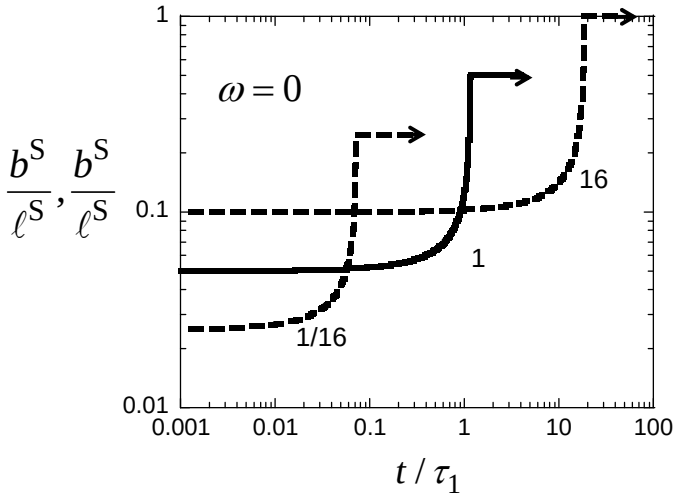

(b)

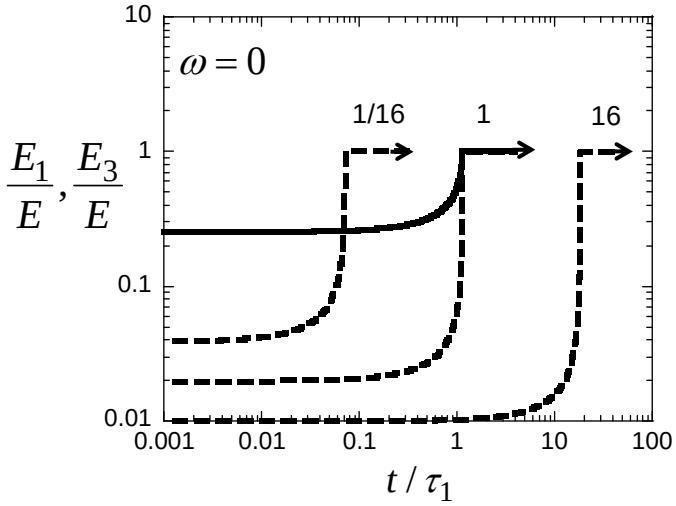

(c)

Fig 5. Free sintering of an APS coating for $\omega = 0$. The numbers on the plots correspond to the values of τ_2 / τ_1 used in the simulations. (a) In-plane, E_{11} (continuous lines) and out-of-plane, E_{33} (dashed lines) strains. (b) Normalised asperity radii on the sides (continuous line) and tops (dashed lines) of the splats. (c) Normalised in-plane, E_1 (continuous line) and out-of-plane, E_3 (dashed lines) moduli.

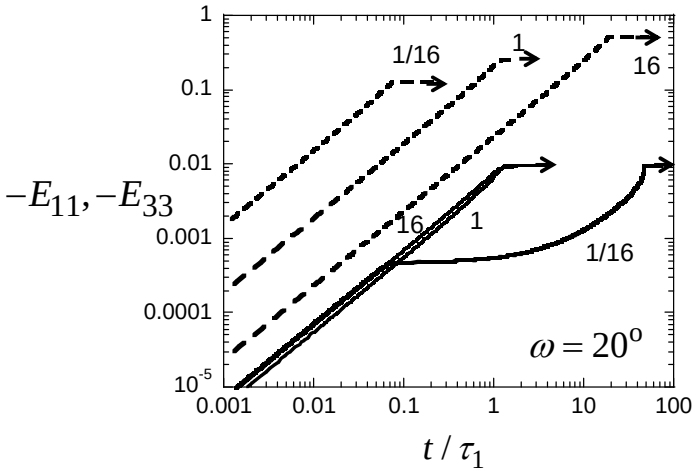

(a)

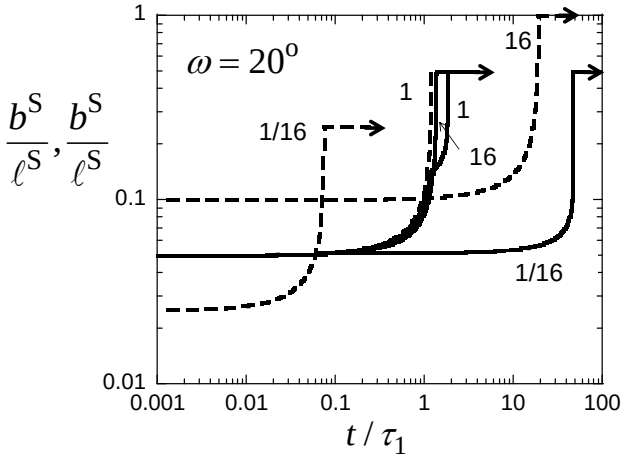

(b)

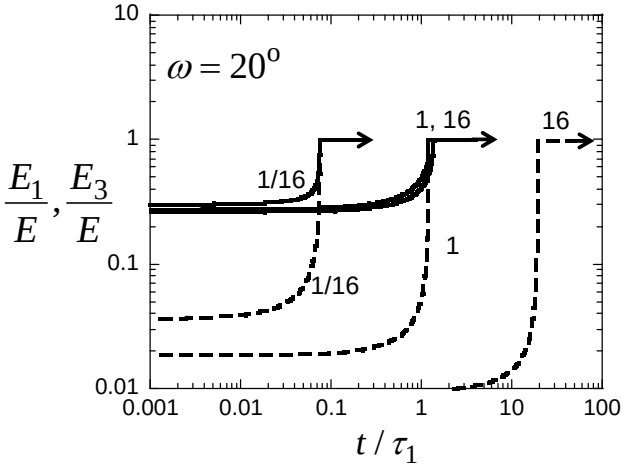

(c)

Fig 6. Free sintering of an APS coating for $\omega = 20^{o}$. The numbers on the plots correspond to the value of τ_2 / τ_1 used in the simulation. (a) In-plane, E_{11} (continuous lines) and out-of-plane, E_{33} (dashed lines) strains. (b) Normalised asperity radii on the sides (continuous line) and tops (dashed lines) of the splats. (c) Normalised in-plane, E_1 (continuous line) and out-of-plane, E_3 (dashed lines) moduli.

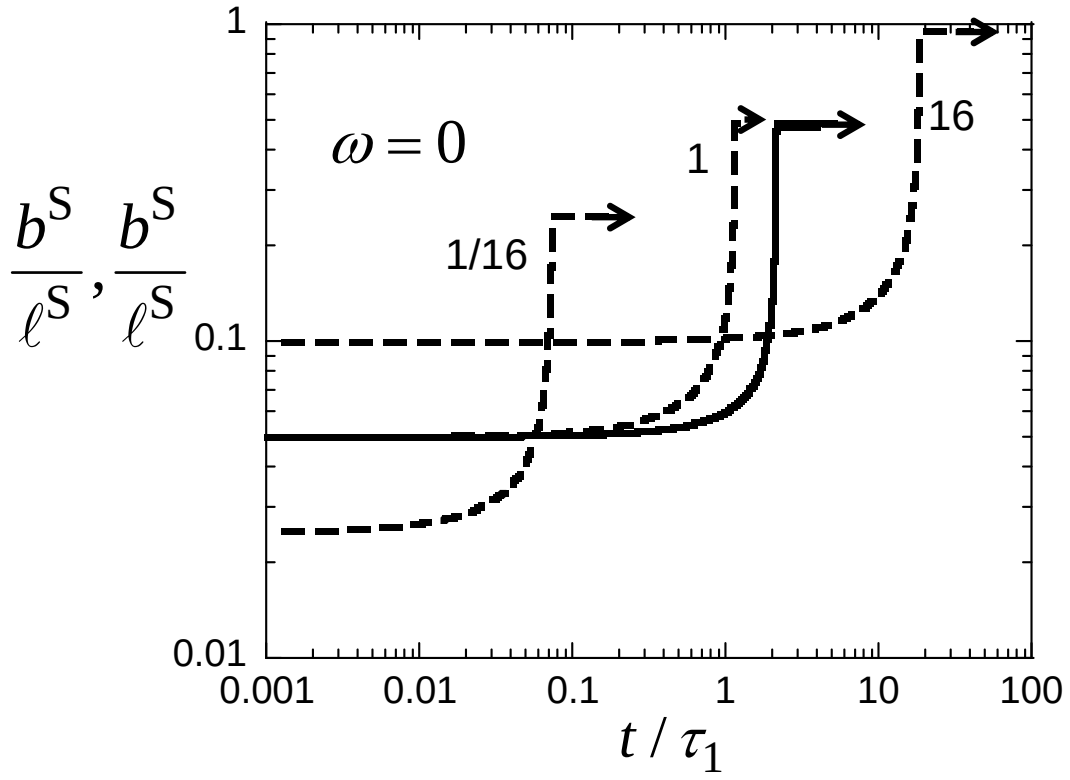

Fig 7. The influence of τ_2 / τ_1 on the constrained sintering of an APS coating for $\omega = 0$ and $\tau_4 / \tau_3 = 4.26$. The continuous line represents the evolution of b^S / ℓ^S and the dashed lines the evolution of b^T / ℓ^S.

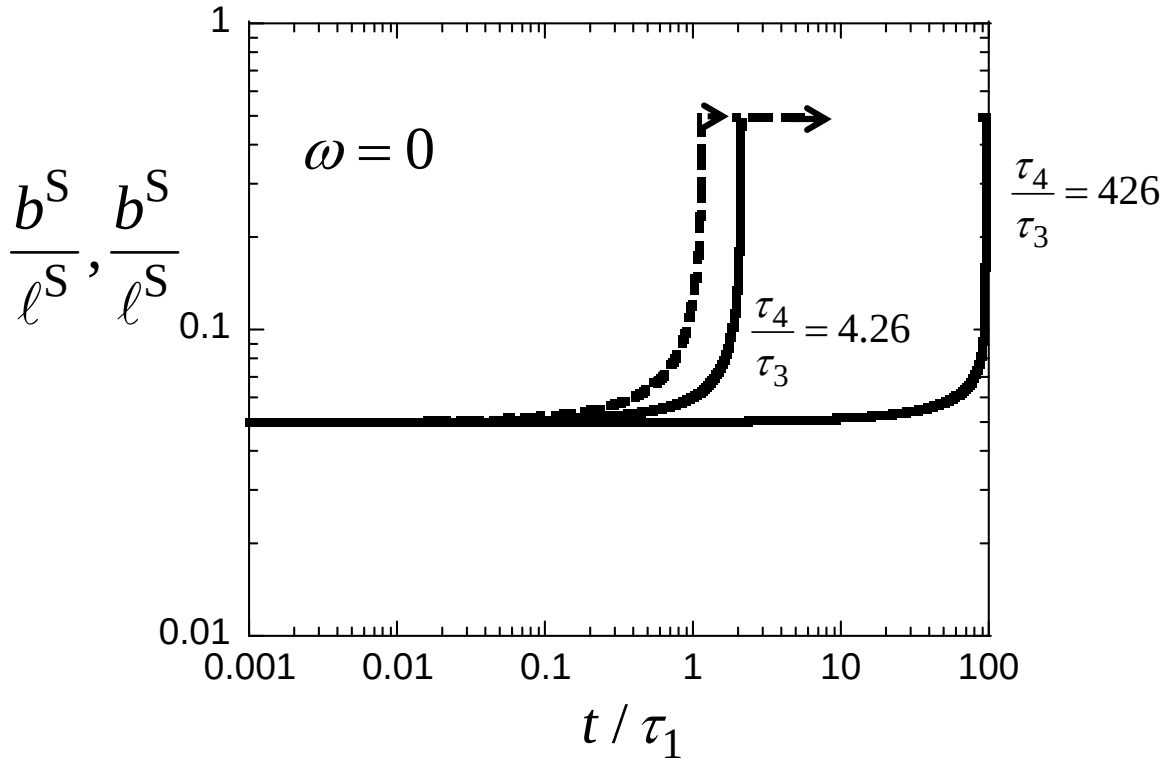

(a)

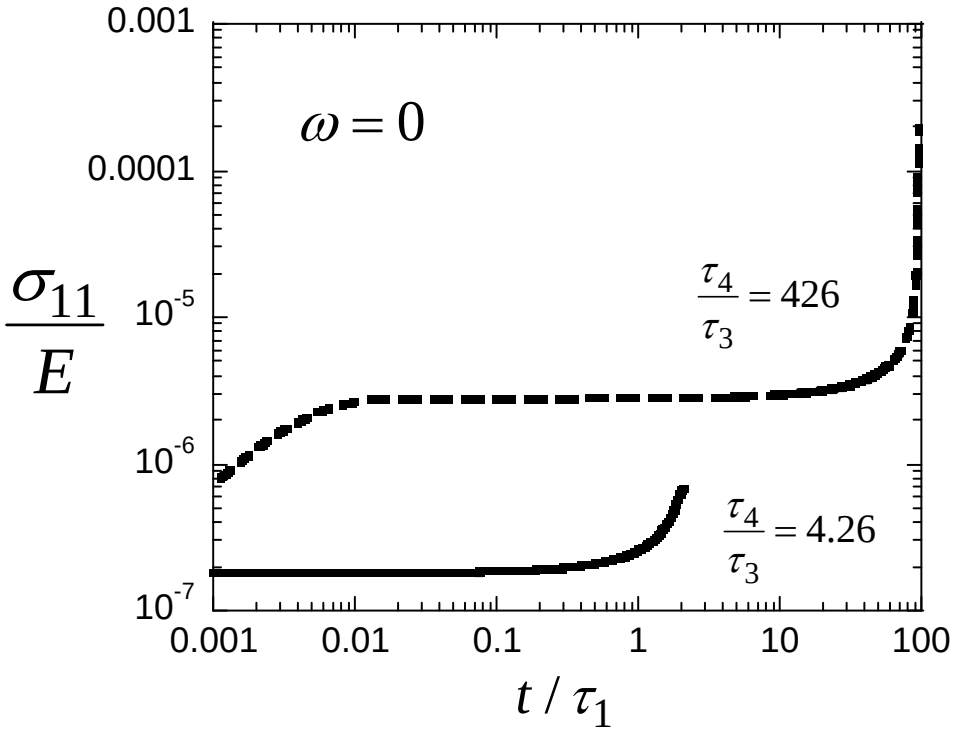

(b)

Fig 8. The influence of τ_4 / τ_3 on the constrained sintering of an APS coating for $\omega = 0$. (a) Normalised asperity radii on the sides (continuous line) and tops (dashed lines) of the splats. (b) Normalised in-plane stress.

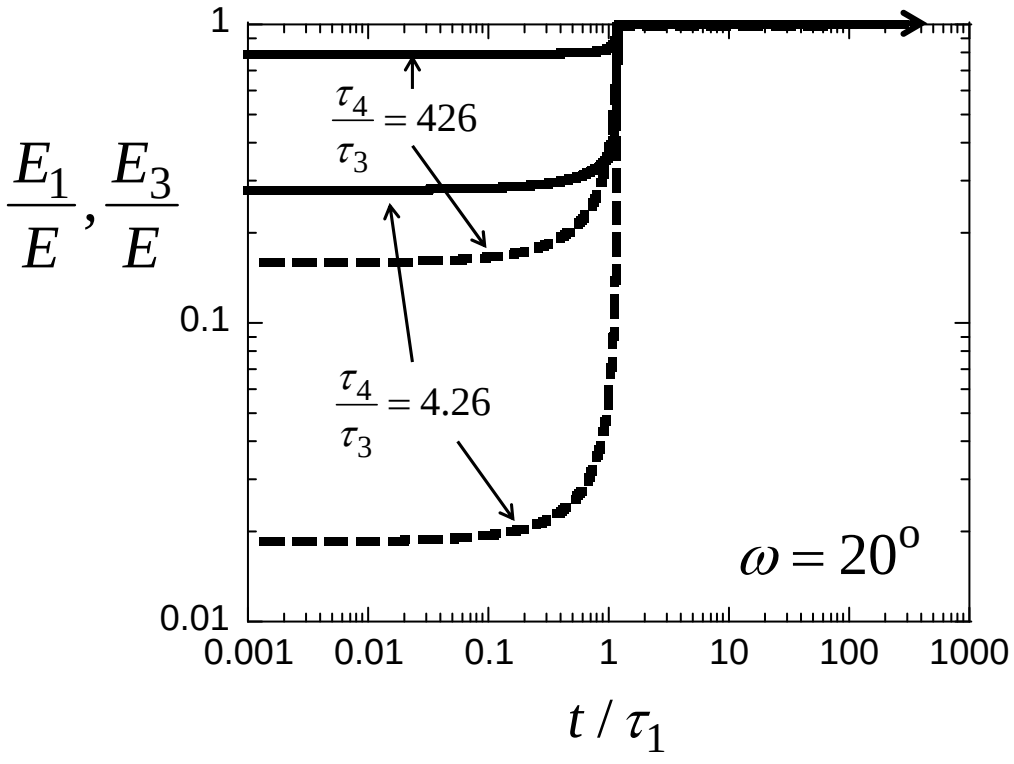

(a)

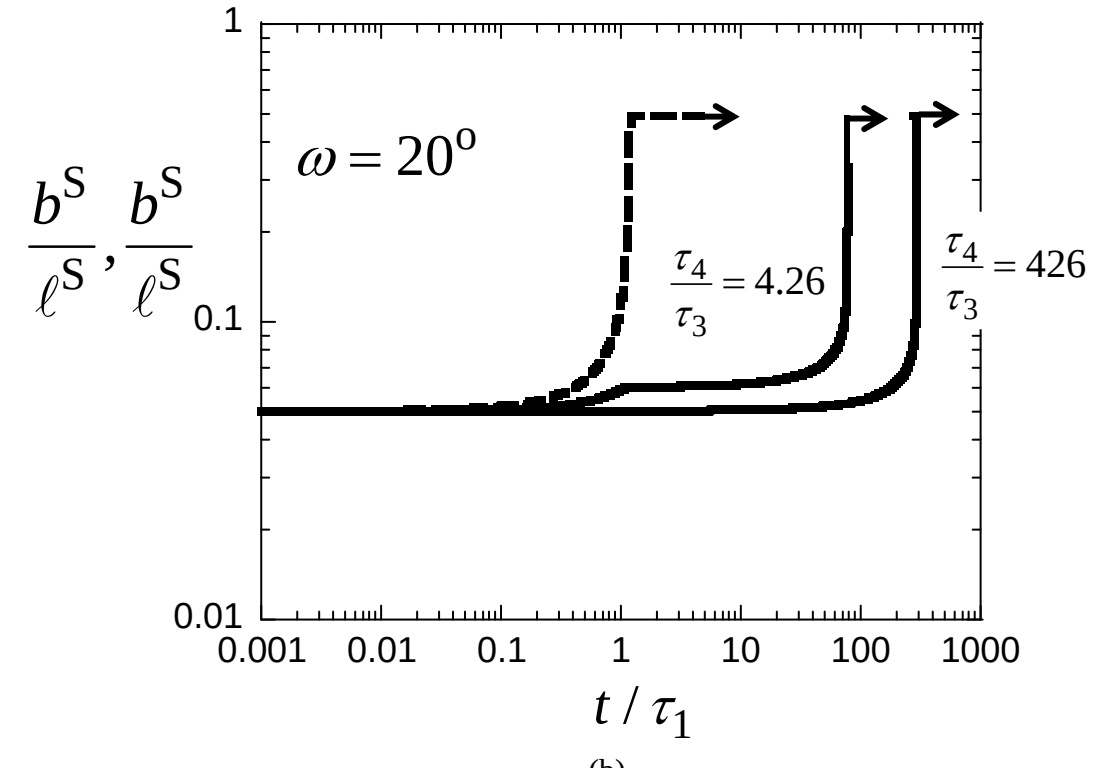

(b)

Fig 9. The influence of τ_4 / τ_3 on the constrained sintering of an APS coating for $\omega = 20^{\circ}$. (a) Normalised asperity radii on the sides (continuous lines) and tops (dashed line) of the splats. (b) Normalised in-plane, E_1 (continuous lines) and out-of-plane, E_3 (dashed lines) moduli.